# Long-Lived Bubbles and Their Impact on Underwater Acoustic Communication

Gabriel Chua, *Student Member, IEEE*, Mandar Chitre, *Senior Member, IEEE*, and Grant B. Deane

***Abstract*—The impact of bubbles on underwater acoustic communication has mostly been studied in environments with strong winds (>12 m/s), and it has been found that the main impact is the strong attenuation due to dense bubble clouds. Without continuous replenishment during high winds, these dense bubble clouds dissipate rapidly in a few minutes, along with the strong attenuation. We find that after the dense bubble clouds dissipate, they leave behind a diffused bubble cloud with very small bubbles. The lifetime of this diffused bubble cloud is much longer than that of the dense bubble cloud. The attenuation due to these residual bubbles is small, but they result in an increase in channel variability due to their random motion. Furthermore, because they can be transported by currents to distant locations, we argue that these bubbles have a more persistent impact in many environments, including ones where winds are not very strong, but there are other sources of bubbles (e.g., shipping channels). We give a statistical characterization of the propagation through these bubbles, and show the impact on acoustic communications with experimental data.**

***Index Terms*—Bubble plumes, underwater acoustic communication, underwater acoustic propagation.**

## I. Introduction

IMMEDIATELY after bubble injection by a breaking wave event, the attenuation can be as high as 50 dB/m [1], practically blocking any signal transmission. The lifetime of these dense bubble clouds is very short—a few seconds to a few minutes [2]. During high winds, waves break frequently and cause a continuous replenishment of these dense bubbles. The Hall–Novarini model [3] assumes that the bubble clouds are time invariant and are only dependent on wind speed. Current literature on the impact of bubbles on underwater acoustic communication relies on simulations based on the Hall–Novarini bubble model. In [4], Boyles *et al.* assumed a “time-frozen” dense bubble cloud (termed the $\beta$-plume) and compute the attenuation for an acoustic propagation through such a plume. As the $\beta$-plume consists of a large number of bubbles, with some in resonance with the acoustic frequency being transmitted, the authors concluded that the attenuation and sound refraction are the dominant effects of bubbles on underwater acoustic propagation. Saraswathi *et al.* [5] also assumed a time-invariant bubble density for the $\beta$-plume. They computed a constant attenuation and sound speed change, which were fed into simulation models to compute the communication performance. The simulation result thus showed that the high attenuation and sound refraction had a large impact on the performance of communication systems. In [6], Mandal *et al.* also assumed a time-invariant bubble density for the $\beta$-plume, and computed a constant attenuation and sound speed change. They evaluated the performance of their communication system based on this time-invariant and range-invariant bubble density, with a horizontal spatial extent of $200\,\mathrm{m} \times 200\,\mathrm{m}$. It is not mentioned as to why the $\beta$-plumes might grow to such a large size, whereas the Hall–Novarini model only suggestted a 50-m$^2$ spatial extent for the $\beta$-plume. They nevertheless concluded that the attenuation had a large impact on the signal-to-noise ratio (SNR), and consequently, packet error performance. Dol *et al.* [7] and Boyles *et al.* [8] also reached the same conclusions that the attenuation and sound refraction from the dense bubbles have the most impact on communication during periods of high wind.

All these works implicitly assume that the acoustic rays would propagate directly through the bubble plume. However, how the rays interact with the bubble plume is dependent on the geometry of the channel. There are experimental observations where the communication performance actually improves when the dense bubbles completely screen off the surface arrival, causing the channel to be more benign [9, Fig. 8].

Without continuous replenishment, the dense bubble clouds that cause high attenuation disappear in a few seconds to minutes [10]. However, some studies have observed frequency-dependent scattering loss at lower wind speeds (around 4 m/s), for periods longer than the lifetime of the dense bubble clouds [11]–[13]. In our controlled experiment, we observe that this loss is due to very small bubbles (<100 $\mu$m) suspended in the water column, which slowly dissolve into the water. Their lifetime is governed by dissolution, a much slower process than the buoyancy process that leads to the rapid loss of larger bubbles. These suspended bubbles have the potential to stay for hours and impact communications at this time scale. As they are randomly transported by turbulence, they act as moving scatterers, causing an increase in the variability of signals propagating through water. The resulting channel is a scattering medium with an elevated variability in terms of phase and amplitude. We provide a statistical characterization of the variability in

Manuscript received April 8, 2020; revised August 23, 2020; accepted September 28, 2020. This work was supported in part by ONR under Grant N00014-17-1-2633. This article was presented in part at the Underwater Communications and Networking 2018 (UComms18), Lerici, Italy, Aug. 2018. *(Corresponding author: Gabriel Chua.)*

**Associate Editor: C. Tsimenidis**.

The authors are with the Department of Electrical and Computer Engineering, National University of Singapore, Singapore, 119222, Singapore (e-mail: chuayuhan1985@gmail.com; mchitre@ieee.org; gdeane@ucsd.edu).

Digital Object Identifier 10.1109/JOE.2020.3028396

terms of its amplitude and phase distribution and as well as time correlation.

As the performance of underwater phase-coherent communication is known to be severely impacted by the phase and amplitude instability of the channel, an adaptive decision feedback equalizer (DFE) with a phase-locked loop is often used to mitigate such a channel impairment [14]. Since environmental factors contribute to the channel variability, the adaptive DFE has been applied in multiple scenarios to assess the impact of various environmental factors, such as the impact of temperature fluctuations [15], wind conditions [16], tidal cycles, and ships [17] on communications. As these residual bubbles contribute to the channel variability, we quantify the performance drop of the equalizer in the presence of these bubbles. Additionally, we observe time correlations of the channel on a time scale of 10–100 s, corresponding to inhomogeneous bubble volumes being advected across the communication channel. As these variations are on the time scales of minutes, which are many times higher than the round-trip time of a communication link within a few kilometers range, we suggest that adaptive techniques may be able to mitigate some of the ill effects of bubbles. In our previous work [18], we examined the lifetime of these long-lived bubbles. In this work, we expand the analysis on bubble lifetime and present results from another experiment to examine the lifetime of these bubbles. We also discuss the factors that determines the persistence of these bubbles. We subsequently show that the rapid channel variation is the more long-lasting impact, and provide a statistical characterization of this impact.

This article is organized as follows. In Section II, we present the theoretical background. In Section III, we describe an experiment in the wind-wave channel at Scripps Institute of Oceanography (SIO), La Jolla , CA, USA and present the bubble measurement results. In Section IV, we present results from a second experiment to validate the lifetime of the residual bubbles. In Section VI, we discuss the impact of bubbles on communication systems. In Section VII, we describe the large-scale bubble motion observed in the SIO experiment. Finally, in Section VIII, we present conclusions.

## II. Theoretical Preliminaries

We present a brief introduction to bubble acoustic theory to facilitate an understanding of the work presented in the rest of the article. In the classical treatment of bubble acoustics, each bubble is treated as a harmonic system of its own. The bubble's radius determines its response toward any incident acoustic frequency. As each bubble is modeled as a damped harmonic system, one can use the following differential equation to examine the response of each bubble to an incident frequency $\omega$:

$$\frac{d^2 r}{dt} + 2\delta\omega_r \frac{dr}{dt} + \omega_r^2 r = Ae^{j\omega t} \tag{1}$$

where $r$ is the radial motion of the bubble wall at its equilibrium value. The relationship between bubble radius $a$ and radial motion $r$ is well described in [19, pp. 294–296]. Furthermore, $\omega_r$ is the resonance frequency of the bubble, $\delta$ is the damping constant, and $A$ is the amplitude of the incident sound. The derivations of the damping constant $\delta$ and resonance frequency $\omega_r$ are well understood [20, pp. 199], [21, pp. 292]. $\omega_r$ is the Minnaert's resonance frequency given by

$$\omega_r = \frac{1}{2\pi a}\left[\frac{3\gamma_h P_h(1+\frac{2\sigma}{P_h a}) - \frac{2\sigma}{a}}{\rho}\right]^{1/2} \tag{2}$$

and $\delta$ is given by [21, eq. (8.2.29) in p. 299]. The physical constants used to calculate $\omega_r$ and $\delta$ are given in Table I.

TABLE I
Typical Values for Physical Constants

| Symbol | Parameter | Value |
|---|---|---|
| $c$ | Sound speed | 1520 m/s |
| $\rho$ | Density of water | 1022 kg/m$^3$ |
| $\sigma$ | Surface tension | 0.0724 N/m |
| $\gamma_h$ | Gas polytropic index | 1.4 |
| $D_t$ | Thermal diffusivity | $2.08 \times 10^{-5}$ m$^2$/s |
| $P_h$ | Hydrostatic pressure at bubble wall | 101325 Pa (near the surface) |
| $\mu$ | Viscosity of water | 0.00102 Pa/s |

### A. Acoustic Cross Section for a Single Bubble and Attenuation By a Multitude of Bubbles

The loss in acoustic intensity for one bubble as a function of bubble radius and incident acoustic frequency is quantified in the extinction cross section [21, p. 201]

$$\sigma_e(a,\omega) = 4\pi\frac{|P_e|^2}{|P_i|^2} = \frac{4\pi a^2(\delta(a,\omega)/\delta_r(a))}{[(\omega_r(a)/\omega)^2 - 1]^2 + \delta(a,\omega)^2} \tag{3}$$

where $P_i$ is the incident pressure (input), $P_e$ is the extinct pressure (output). $\sigma_e$ is dependent on the incident frequency, damping constant, and resonance frequency. $\delta_r(a)$ in (3) is the resonant damping constant $\delta(a,\omega_r)$. Acoustic waves propagate through a multitude of bubbles of various sizes; as a result, the extinction cross section is aggregated over the distribution of bubbles $n(a)$, to give the scattering cross section per unit volume $S_e$

$$S_e(\omega) = \int_{a_{\min}}^{a_{\max}} \sigma_e(a,\omega)n(a)da. \tag{4}$$

Attenuation per unit distance (also referred to as absorption) is given by [21, eq. (8.3.18) in p. 315]:

$$\alpha_b(\omega) = 4.34 S_e(\omega)\ \text{(dB/m)}. \tag{5}$$

### B. Inversion and the Choice of Acoustic Frequencies

Equation (4) is the forward model, it indicates the amount of attenuation to expect as a function of bubbles population. To obtain the bubble population from attenuation, one needs to perform an inversion of the forward model. One can see that (4) can be written as a linear system in a discrete form when discrete

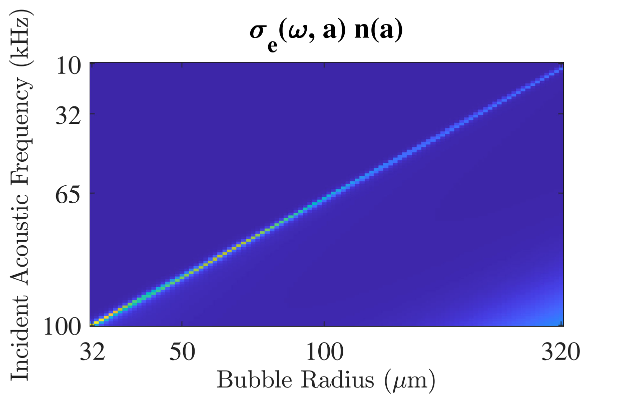


Fig. 1. Acoustic cross section evaluated with a power law bubble density. $n(a) = n_0 a^{-n_p}$, $n_p = 4$, and $n_0 = 10^{-12}$ with respect to the input variables, bubble radius $a$, and incident acoustic frequency $\omega$.

acoustic frequencies are used to probe the bubbles

$$\begin{bmatrix} \alpha_b(\omega_1) \\ \alpha_b(\omega_2) \\ \dots \\ \alpha_b(\omega_n) \end{bmatrix} = \begin{bmatrix} S_e(a_1,\omega_1) & \dots & S_e(a_m,\omega_1) \\ S_e(a_1,\omega_2) & \dots & S_e(a_m,\omega_2) \\ \vdots & \ddots & \vdots \\ S_e(a_1,\omega_n) & \dots & S_e(a_m,\omega_n) \end{bmatrix} \begin{bmatrix} n(a_1) \\ n(a_2) \\ \dots \\ n(a_m) \end{bmatrix}. \tag{6}$$

If the acoustic frequencies are chosen on a log scale, the matrix in (6) becomes a diagonal matrix [22] as shown in Fig. 1. This results in a simple inversion scheme, called the resonance bubble approximation

$$n(a) = \frac{\alpha_b(\omega)\delta(a,\omega)}{85.7a^3} \tag{7}$$

where $\alpha_b(\omega)$ is absorption measured in dB/m at incident frequency $\omega$ and $n(a)$ is the bubble density spectra in number of bubbles/m$^3$/$\mu$m. This approximation has been applied in [23]–[28] and was found to give accurate results.

### C. Quantifying Bubble Lifetime Through Void Fractions

Bubbles are created within a cloud with a range of initial radii. The radii vary over time as bubbles dissolve or experience a range of hydrostatic pressures as they rise or fall. Tracking of the size of each individual bubble across time is difficult. Instead, void fraction is commonly used as a quantity to characterize the bubble population as a whole. The void fraction is an integration of the gas content from all the individual bubbles present in the measurement volume. It is defined as

$$\eta(t) = \frac{4}{3}\pi \int_{a_{\min}}^{a_{\max}} n(a,t)\, a^3\, da \tag{8}$$

where $n(a,t)$ is the time-dependent bubble density spectra $n(a)$, whereas $a_{\min}$ and $a_{\max}$ are the minimum and maximum bubble radii taken into calculation. We define the collective lifetime of the bubbles (or equivalently, the lifetime of the bubble cloud) as the time from which they were injected until the time at which the void fraction falls below a specified threshold. We choose a threshold of $10^{-8}$, as it is the lower limit of the acoustic inversion technique [29].

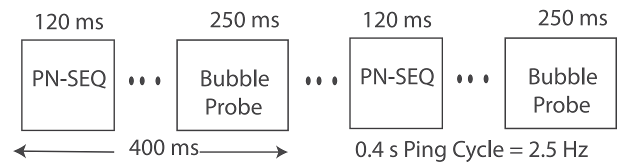


Fig. 2. Interleaved structure of the bubble probes and the PN sequences.

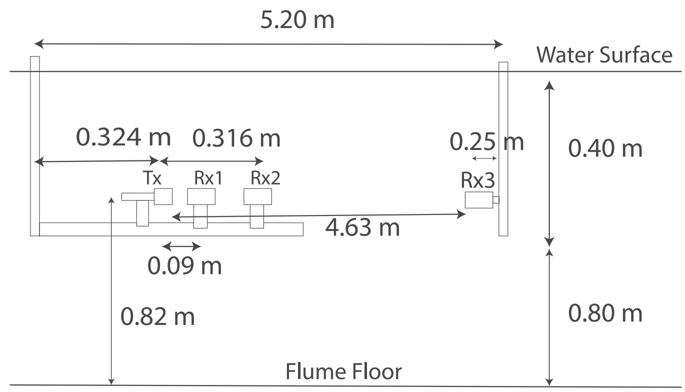


Fig. 3. Schematic of the experimental setup. Tx is the projector used to transmit acoustic signals, and Rx1 and Rx2 are the receiving hydrophones for estimation of bubbles. Rx3 is an additional receiving hydrophone located further in the channel.

## III. Wind-Wave Flume Experiment

### A. Objectives

We designed an experiment to answer the following questions.

1) What is the lifetime of bubbles that affect the frequencies (10–30 kHz) typically used for medium-range communications?
2) What is the impact of these bubbles on communication?

### B. Experimental Setup

We conducted the experiment in the wind-wave flume at the SIO. The facility allowed us to generate wind-driven breaking waves similar to those found on wind-driven surfaces. To measure bubbles, we instrumented the channel with an ITC1032 projector to transmit short narrowband pulses (bubble probes). We used three ITC6050 C hydrophones as receivers. Additionally, we generated broadband pseudorandom noise (PN) sequences spanning the frequency band of interest, and interleaved them with the bubble probes. These were used to characterize the communication channel in Section VI. The interleaved structure is shown in Fig. 2. We show the schematic of the setup in Fig. 3 and an example of how an injection was created is shown in Fig. 4.

### C. Signal Design

We sent sinusoidal pulses of discrete frequencies modulated using a tapered cosine window with tapers of 0.1. Each pulse was 10 ms in duration, and a total of 25 frequencies in the range of 16–86 kHz were concatenated back to back; the concatenation of the 25 pulses was referred to as the bubble probe as shown in Fig. 2. The frequency spacing for the inversion of the bubble

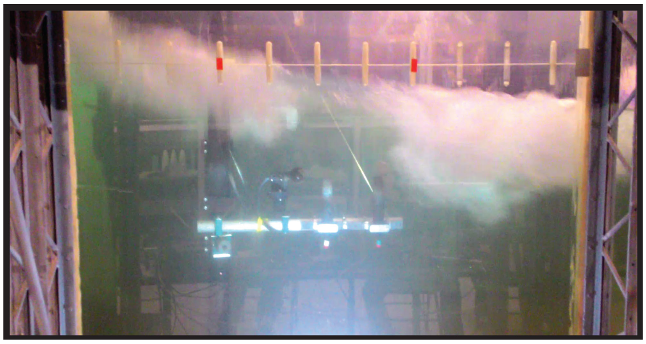

Fig. 4. Side view of the wind-wave channel showing the bubble characterization system and bubble clouds induced by a breaking wave. The wave is propagating from right to left and was induced to break by 15-m/s airflow in the sealed channel headspace.

density over the chosen frequency band was optimized using the method suggested in [22]. We computed a void fraction estimate by first computing the bubble density time evolution $n(a, t)$ from $\alpha_b(\omega, t)$ with (7), where $t$ is the time index of the bubble probe. Subsequently, we integrated the bubble density to obtain the void fraction $\eta$ with (8). The calculation of $\alpha_b$ is described in Section III-D. The void fraction estimates were obtained at a rate of 2.5 Hz.

### D. Absorption Calculation

We calculate absorption $\alpha_b$ as

$$\alpha_b(\omega_i) = -\frac{1}{d} \ln A(\omega_i) \tag{9}$$

where $\omega_i$ is the center frequency of each sinusoidal pulse, $i$ is the index in the set of frequencies, and $d$ is the distance between the transmitter and receiver. As $\alpha_b$ has units of Nepers per meter, we multiply a factor of 4.34 to convert it into dB/m. $A(\omega_i)$ is calculated from

$$\left| \frac{X_{\text{bubbles}}(\omega_i)}{X_{\text{no bubbles}}(\omega_i)} \right|$$

where $X_{\text{bubbles}}(\omega_i)$ is the received spectrum of the sinusoidal pulse at its center frequency when there are bubbles and $X_{\text{no bubbles}}(\omega_i)$ is the received spectrum of the sinusoidal pulse at its center frequency when there are no bubbles.

### E. Results and Discussion

*1) Void Fraction Measurements:* Although the void fraction is derived from bubble density estimates, we present the void fraction results first, and the bubble density later in Section III-E.2. We present void fraction results from two runs of the experiment in Fig. 5. Each run lasted for 40 min, and the time gap between two runs was 15 min. The sequence of events and the corresponding stage of the bubble lifetime are shown in Table II. We start the description from the first run at Stage A. In the beginning, the wind-wave channel was completely at rest (no wind and waves) and there were no bubbles. The small apparent increase in void fraction at around 2 s in the "First Run" panel of Fig. 5 seen during Stage A was due to electrical noise injected into the recording system when the wave generation paddle was briefly switched on and off. At Stage B, we switched on the paddle to produce waves. This generated 0.35-m amplitude surface waves at a frequency of 0.7 Hz. There is a small estimated $\eta$ of $10^{-8}$ due to random turbulent motions generated by the waves, due to the increased acoustic noise due to the machinery noise. Next, in Stage C, the wind was turned on. The waves started to break and bubbles were injected and thus the void fraction surged. The estimated void fraction is a little less than $10^{-4}$. This is less than $10^{-2}$ as reported in $\beta$ plumes, as we are only tracking bubbles in the range of 200 $\mu$m and below. The void fraction contribution of bubbles larger than 200 $\mu$m is not included in our estimates, because we did not transmit probe signals resonant with these larger bubbles. As we are not interested in characterizing the dense bubble clouds, obtaining the actual void fraction in the dense bubble clouds is not of crucial importance to our experiment.

TABLE II
STAGES OF EXPERIMENT

| Stage | Wave | Wind | Channel State |
|---|---|---|---|
| $A$ | off | off | Channel at rest |
| $B$ | on | off | Only waves are on |
| $C$ | on | on | Injection phase |
| $D$ | on | off | Buoyancy dominated phase |
| $E$ | on | off | Dissolution dominated phase |

TABLE III
PARAMETER VALUES FOR VOID FRACTION DECAY

| - | $\eta_0^{\text{bouy}}$ | $\eta_0^{\text{disso}}$ | $\Gamma_{\text{buoy}}$ | $\Gamma_{\text{disso}}$ |
|---|---|---|---|---|
| Run 1 | $10^{-4}$ | $10^{-7}$ | 0.02 | 0.002 |
| Run 2 | $10^{-4}$ | $10^{-7}$ | 0.02 | 0.001 |

After bubble injection in Stage C, we turned off the wind and the injection stopped (Stage D). The void fraction decayed rapidly due to loss of bubbles due to buoyancy. We fit an exponential decay to the decreasing trend of void fraction during the buoyancy dominated stage

$$\eta(t) = \eta_0^{\text{bouy}} e^{-\Gamma_{\text{buoy}} t} \tag{10}$$

where $\eta_0^{\text{bouy}}$ is the initial void fraction at the injection and $\Gamma_{\text{buoy}}$ is the buoyancy decay constant. This is performed with least-squares fitting. The results are tabulated in Table III. The buoyancy decay constant is identical for both runs, suggesting that the buoyancy process is consistent during the two runs. After the buoyancy dominated phase, the decay rate changes dramatically, signaling a change in the regime of bubble loss. The decay after this time is mostly due to the dissolution of the bubbles. We also model the void fraction decay in this stage as an exponential decay with

$$\eta(t) = \eta_0^{\text{disso}} e^{-\Gamma_{\text{disso}} t} \tag{11}$$

where $\Gamma_{\text{disso}}$ is the dissolution decay constant. The dissolution decay constant fitted is much smaller than the buoyancy decay

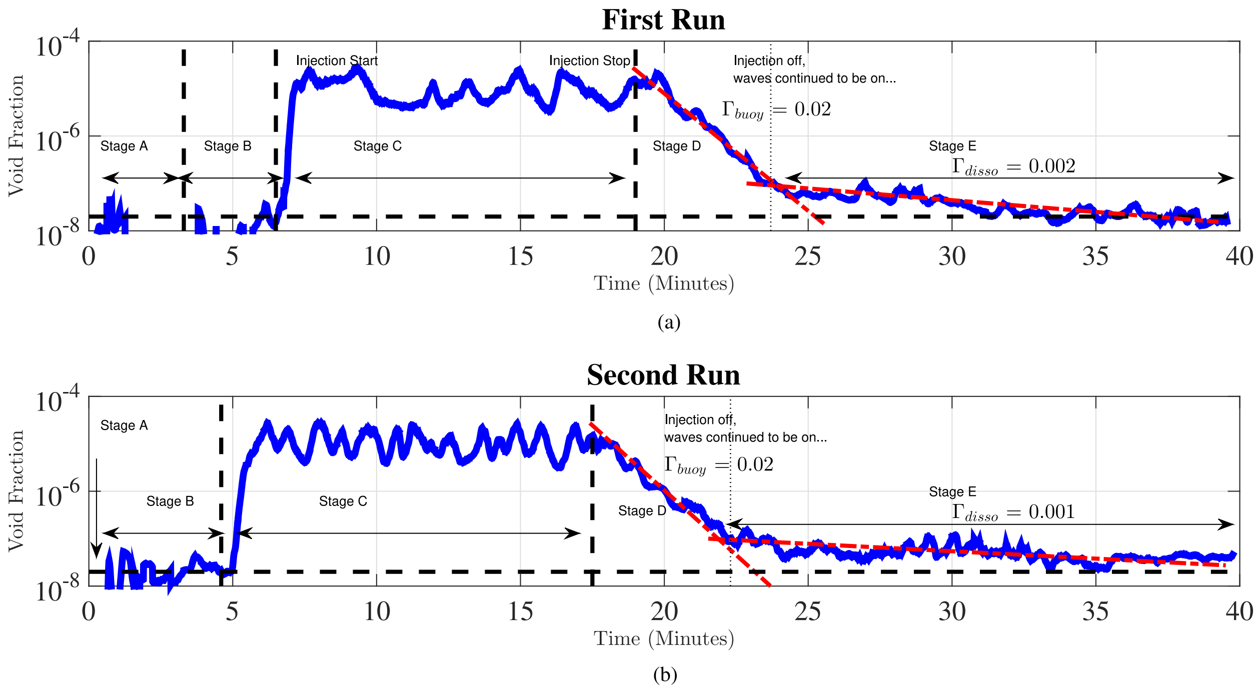


Fig. 5. Void fraction as a function of time. The solid lines are the experimental data and the dashed lines are the fitted exponential decaying trends. (a) First experiment run. (b) Second experiment run.

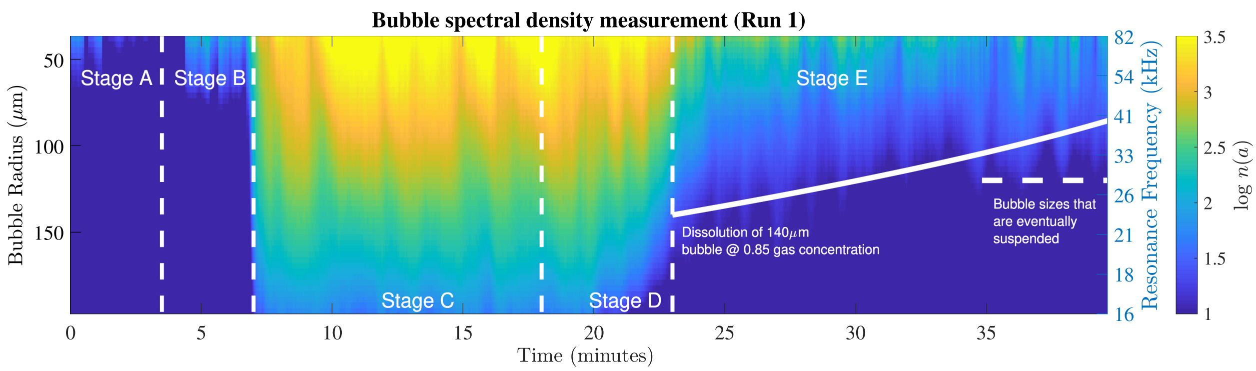


Fig. 6. Bubble spectral density measurement from the first run. On the left vertical axis is the bubble size, and on the right vertical axis is the corresponding resonance frequency of the bubble. The white solid line is the evaluation of (12) of a 140-$\mu$m bubble at 0.85 dissolve gas saturation ratio.

constant, one can see that the dissolution process lasts much longer than the buoyancy process. The second run shown in Fig. 5(b) shows the same overall features as the first run with the exception that the dissolution decay constant during the second run is approximately half the value seen in the first run.

*2) Bubble Spectra Measurements:* Figs. 6 and 7 show the bubble spectra as a function of time for the first and second runs, respectively. In the first run, there are few bubbles in Stages A and B. More bubbles are seen in Stage C. In Stage D, larger bubbles are lost due to buoyancy. Subsequently, in Stage E, we can see the loss mechanism of the bubbles starting to change. Bubbles smaller than a particular size are suspended by wave-induced turbulence. During this stage, the bubbles dissolve, and their radii decrease over time due to gas diffusing out from the bubbles. During the second run, in Stage B, we see some leftover bubbles from the previous run. In Stage D, the trend is similar to the first run. In Stage E, we observe that the bubbles dissolve more slowly than they did in the first run.

*3) Dissolution Analysis:* Next, we analyze the bubble dissolution process. The bubble dissolution process is well captured by Epstein and Plessets' equation [30]

$$\frac{da}{dt} = -D\frac{1-\gamma+\frac{2\sigma}{P_a a}}{1+\frac{4\sigma}{3P_a a}}\left[\frac{\chi}{a}\right] \tag{12}$$

where $\chi = RT/K_H$. The parameters in (12) are defined in Table IV. This model is a differential equation that gives the radius of a single bubble with respect to time as it dissolves in water. Specifically, it predicts the reduction in the size of a single bubble due to air diffusing through the air–water boundary of

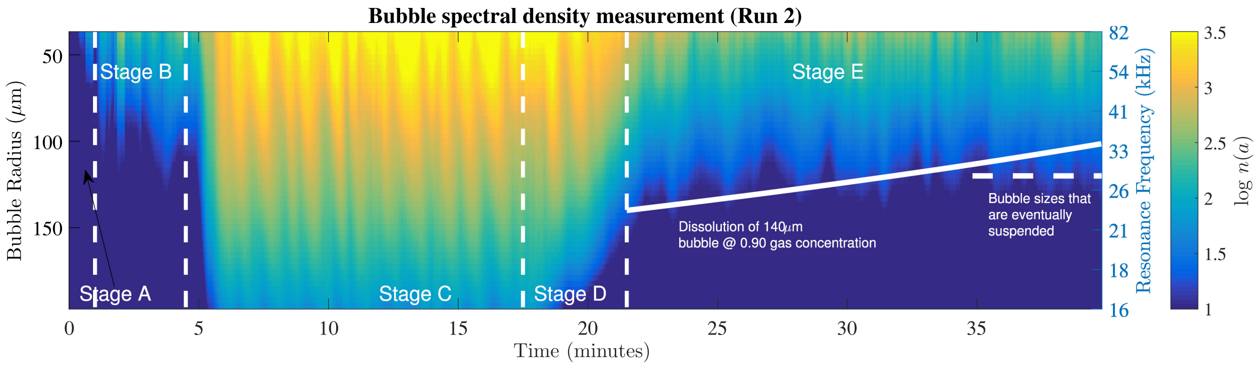


Fig. 7. Bubble spectral density measurement from the second run. The white solid line is the dissolution curve from (12) at 0.90 dissolve gas concentration, showing the modeled largest bubble size as a function of time.

TABLE IV
TYPICAL PHYSICAL PARAMETER VALUES IN (12)

| Symbol | Parameter | Value |
|---|---|---|
| $D$ | Diffusivity of air in water | $2\times10^{-9}$ m$^2$/s |
| $\sigma$ | Surface tension | 0.0724 N/m |
| $R$ | Universal gas constant | 0.08206 atm/(mol K) |
| $T$ | Temperature | 293 K |
| $K_H$ | Henry's law constant | 1614 atm mol |
| $\gamma$ | Dissolved gas saturation ratio | 0.85, 0.9 |
| $P_a$ | Atmospheric pressure | 1 atm |

the bubble as time passes. Although the model only accounts for a single component of gas, this model has been verified to be sufficiently accurate in clean water (without surfactants) for the bubble sizes we are interested in [31]. One of the key assumptions of the model is a "clean" surface on the bubble without a layer of coating on the boundary between air and water. The presence of surfactants that coats on the bubble can potentially prolong their lifetime. Furthermore, in the case of particulates, it can cause the bubbles to persist indefinitely [32].

To validate the premise of a dissolution dominated trend in Stage E, (12) is evaluated to predict the maximum bubble size observable $a_{\max}(t)$ as the bubbles dissolve. We perform the evaluation with a fourth-order Runge Kutta method with typical parameter values as shown in Table IV. We use 0.85 for $\gamma$, as this is a typical value for the dissolved gas saturation for the temperature on that day (293 K) [31].

The decrease in radius over time of an initially 140-$\mu$m bubble is overlaid on our bubble measurement results as shown in Fig. 6 (Stage E). We find an agreement of the theory and measurement from the 23rd to the 35th minute, suggesting that the bubbles are indeed dissolving. However, after the 35th minute, we find that the bubbles stop dissolving and are stabilized. This could be due to surfactants covering the surface of the bubble and thus preventing air from further diffusing into the water. We refer to these long-lasting small bubbles as the *suspended microbubbles*.

We compare the dissolution trend in both runs. Although the bubbles that are suspended in both runs are 140 $\mu$m and smaller, the rate at which the bubbles reduce in size is a factor of 2 slower in the second run. This is very likely due to a higher starting dissolved gas concentration in the second run. The dissolved gas concentration in the water increased because the bubbles injected in the first run dissolved into the water to become dissolved gas. As the water was then more saturated with gas, subsequent dissolution was slower, and as a result, the bubbles took longer to dissolve. For a quantitative comparison, we compare the measurements with a dissolution trend of a 140-$\mu$m bubble under a 0.9 dissolved gas concentration. We thus evaluate (12) and overlay the dissolution curve on the measurements in Stage E of Fig. 7. We find that the slower dissolution can be completely explained by a higher gas concentration during the second run. Finally, at the end of the experiment, we again observe that the bubbles are stabilized.

An ambiguity regarding comparing the dissolution trend in a multifrequency measurement is that the dissolution of a single bubble against the backdrop of bubble density measurements is somewhat dependent on the color-scale chosen. While the general dissolution trend of all the bubbles present in the system is unmistakable regardless of the color-scale chosen, the ambiguity is inherently due to the uncertainty regarding the largest bubble suspended, which is chosen based on the noise floor defined by the multifrequency measurements. If one were to argue that the noise floor should be slightly higher, the largest bubble suspended would be slightly smaller, so would the decay of the bubble densities over time. If one were to evaluate the bubble dissolution theory with a smaller starting bubble size, in this case, the dissolution trend would still be apparent and not affected by the largest bubble suspended.

*4) Dissolution Lifetime:* In Fig. 8, we show the portion of the dissolution curve that was overlaid on the experiment data. We can easily deduce that the bubbles have not completely dissolved during the experiment. Most of the bubbles that are left are the ones smaller than 100 $\mu$m. Thus, we can deduce that these bubbles can last for 40 min or more after the initial turbulent period, even in the case where there are no significant surfactants in the water.

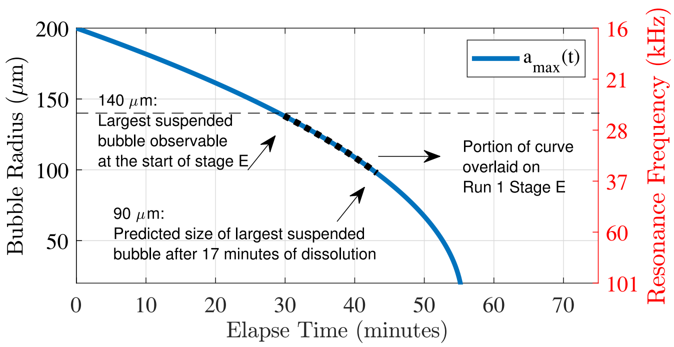


Fig. 8. Theoretical dissolution curve from (12) at a dissolved gas concentration of 0.85. Dotted line is the portion of the theoretical dissolution curve overlaid on the measurement data in Fig. 6.

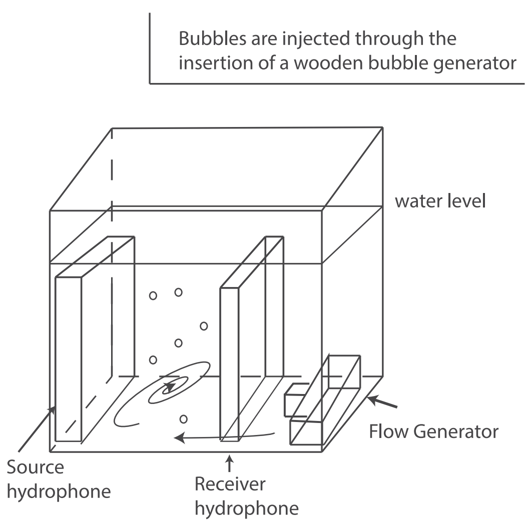


Fig. 9. Experiment setup to measure the lifetime of microbubbles in both clean saltwater and sampled seawater.

## IV. Lifetime of Microbubbles Stabilized in Seawater

To determine the lifetime of the micro-bubbles, we conducted a second experiment. The objective of this experiment was to measure the lifetime of microbubbles in seawater samples from a marina. As a control, we compare the microbubbles' lifetime in artificial "clean" saltwater.

### A. Experimental Setup

The experimental setup is depicted in Fig. 9. We prepared artificial saltwater and sampled seawater from a marina in Singapore. Saltwater was chosen as a control instead of freshwater because it is known that salt would prevent the coalescent of bubbles [33]. Artificial saltwater of 35-ppt salinity was prepared by adding the right amount of salt (NaCl) into tap water. We stirred the solution for 3 h and used a conductivity sensor to confirm the salinity. The conductivity values matched the targeted salinity within 5%.

The experiment was conducted in a metal tank (60 cm $\times$ 30 cm) as shown in Fig. 9. We used a flow generator to simulate ocean turbulence. The flow rate of the flow generator was around 30–35 L/min. An air pump was connected to a wooden bubble generator to generate bubbles. The bubbles generator was chosen because the pore sizes of the wood were in the scale of tens to hundreds of micrometers, roughly corresponding to the size of the bubbles we intended to emulate.

The flow rate of the air pump was around 1–2 L/min. The setup was verified to be able to produce bubbles in the range of 20–200 $\mu$m through an image analysis [34, p. 29]. We inserted the bubble generator into the tank for 5 min to generate bubbles. After this, the bubble generator was removed from the setup, and we observed the decay of the void fraction without further injections. This procedure was repeated five times with new water samples. For bubble measurements, the bubble spectral density and void fraction computations were similar to the procedure as described in Section II. We measured the absorption between two transceivers and inverted for the bubble spectral density and computed the void fractions over time. The tank was cleaned and wiped thoroughly every time the water was changed to avoid contamination. The dissolved gas saturation ratio was always controlled at 100% (or ratio of 1) at the start of the experiment by injecting bubbles and using a dissolved oxygen sensor to measure the dissolved oxygen in the water at the start of every run.

### B. Results

The time-varying decay in void fraction for both natural and artificial seawater experiment are shown in Fig. 10. Bubbles in contamination-free artificial saltwater completely dissolve in 40–75 min, whereas bubbles in sampled seawater can last for 95–160 min. This experiment clearly shows that the bubble lifetime is prolonged by some factor in natural seawater that inhibits dissolution. We see that dissolution theory predicts the dissolution lifetime for pure saltwater well, but cannot predict the lifetime of surfactant stabilize bubbles. In ocean waters near the marina, where surfactants are abundant, the lifetime of the microbubbles can be a few hours.

## V. Discussion

From the experiments and quantitative modeling, we observe that both dissolved gas concentration and stabilizing factors, such as particulates and surface-active compounds, contribute to the longevity of the microbubbles. Given that the lifetime of microbubbles can greatly exceed the time interval between the arrival of two consecutive ships as they pass through in busy shipping lanes (e.g., hours of lifetime as compared to a ship every 5–10 min in Singapore waters), we argue that the microbubbles never truly fade away. The injection rates are much higher than the lifetime of these bubbles. Furthermore, the constant injection of bubbles also drives up the dissolved gas concentration, which causes subsequent injections to last longer than the previous, therefore, making a persistent presence of microbubbles near busy shipping lanes more likely. Of course, the presence of the microbubbles and their spatial extent is not only determined by the lifetime of the bubbles, but also depends on other factors, such as current advections, mixing forces in the ocean, and the vertical distribution of the bubbles. A thorough analysis of these

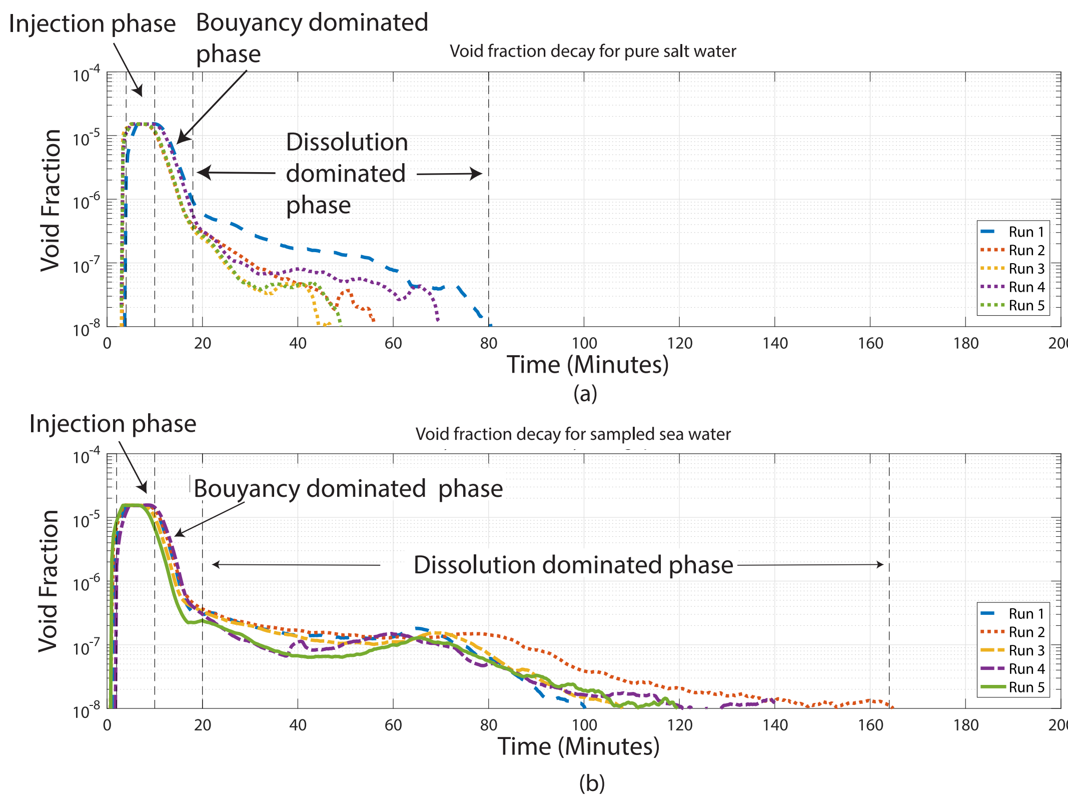


Fig. 10. (a) Void fraction decay for pure saltwater. (b) Void fraction decay for sampled water from a marina in Singapore.

factors is beyond the scope of this article. However, one has to acknowledge that the long life time of the bubbles can have a significant impact on their spatial reach.

We summarize the following key findings from the bubble measurements.

1) After injection, there are a lot of bubbles that last for a few minutes. The attenuation during this period is high.
2) The large bubbles rise up and are rapidly lost, but the smaller bubbles are eventually stabilized. These small bubbles have the potential to last for hours. We refer to them as the *suspended microbubbles*.
3) The suspended microbubble cloud consists of bubble sizes of about 100 $\mu$m and below. The void fraction in these clouds is about $10^{-7}$.

The high attenuation from the dense bubble clouds is confined to the locality of the injection, typically in shipping lanes or in areas with strong winds, and only occurs at times immediately following the injection occurs. What is most likely to be experienced by typical underwater acoustic communication channels is the dissolution dominated phase (Stage E). This is because, during this phase, the bubbles are diffused and can be carried (advected by currents) to locations that are distant from their injection point. The spatial scale of the suspended microbubbles extends as far as the currents can carry them during their lifetimes. As such, we hypothesize that suspended microbubbles present a persistent challenge to communication systems in regions where they can be stabilized and are injected at intervals shorter than their persistence. Thus, we focus on the characterization of the suspended microbubbles next.

## VI. Impact on Communication Systems

### A. Stochastic Nature of the Microbubbles

Acoustic propagation in a bubbly medium can be characterized through the complex wavenumber [35]

$$k_m^2(\omega) = k_0^2(\omega) + \int_{a_{\min}}^{a_{\max}} h(a,\omega)\, n(a)\, da \tag{13}$$

where

- $k_m$ complex wavenumber in the medium;
- $k_0$ wavenumber without bubbles, $k_0 = \omega/c$, $c$ is the bubble-free sound speed;
- $a$ bubble radius;
- $h(a,w)$ scattering coefficient of one bubble of radius $a$ [36];
- $a_{\min}$ and $a_{\max}$ minimum and maximum bubble radii present in the bubble population;
- $n(a)$ bubble spectral density that describes the amount of bubbles as a function of radius per unit volume per unit radius increment.

As the cloud of suspended microbubbles is assumed to consists of a small number of bubbles with a void fraction of around $10^{-7}$, the integral in (13) results in a value that is small compared to the bubble-free wavenumber $k_0$. By moving the $k_0^2$ term in

(13) down to the denominator, we obtain

$$k_m^2/k_0^2 = 1 + \frac{1}{k_0^2}\int_{a_{\min}}^{a_{\max}} h(a,\omega)\, n(a)\, da. \tag{14}$$

Then, moving the square term to the right

$$k_m/k_0 = \left[1 + \frac{1}{k_0^2}\int_{a_{\min}}^{a_{\max}} h(a,\omega)\, n(a)\, da\right]^{1/2}. \tag{15}$$

Equation (15) can be approximated with a Taylor series when the second term is small

$$k_m \approx k_0 + \frac{1}{2k_0}\int_{a_{\min}}^{a_{\max}} h(a,\omega)\, n(a)\, da. \tag{16}$$

Note that $(1+x)^\alpha \approx (1+\alpha x)$ when $x$ is small. Since we know that the bubbles that are suspended are about 100 $\mu$m and smaller, and a 100-$\mu$m bubble resonates at 33 kHz near the surface, it is reasonable to assume that for communication systems that operate at frequencies below 33 kHz, sound absorption driven by bubble resonance is not the dominant propagation effect. The respective resonance frequencies of the suspended microbubbles can be obtained from the right vertical axis of Figs. 6 and 7. One can see that in Stage E, since low-to-mid frequency communication systems are out of the resonance region of the suspended bubbles, the scattering coefficient for bubbles of different sizes shows small values when compared to those bubbles in resonance (see [21, Fig. 8.2.4]). Since the bubbles are already in the nonresonance regime, we assume that as these bubbles dissolve, the change in the scattering coefficient is small as compared to the case if the bubble dissolves and thereby transits from resonance regime to the nonresonant regime. As these subresonance bubbles are randomly advected by turbulence, the number of them interacting with each acoustic path changes with time. This results in a quasi-stationary time fluctuation of the complex wavenumber

$$k_m(t) = k_0 + \Delta k(t) \tag{17}$$

where the fluctuation of the wavenumber $\Delta k$ is due to the random motion of these subresonance scatterers, which have largely uniform scattering coefficients. Since the change in scattering coefficient is small as the bubbles dissolve, we assume that the variation is mostly driven by turbulence. We assume that the statistics of the variation to be stationary for the time frame relevant to communication systems (a few seconds for a packet), as the time coherence of the turbulent motion is on the scale of minutes to hours [37], [38]. To model the stochastic effect of the turbulence, we note that the bubble-free wavenumber $k_0$ is a constant, whereas the variation caused by the turbulence-advected microbubbles $\Delta k(t)$ is random. As such, we can use a stationary random process $R_p(t)$ to model the variation where $R_p(t)$ has a statistical distribution and a power spectral density (PSD) associated with it. The distribution describes the excursion from the mean and the PSD characterizes the time correlation

$$k_m(t) = k_0 + R_p(t). \tag{18}$$

We model the distribution to follow a Gaussian distribution, invoking the central limit theorem to justify the choice. Propagation through a multiplicative concatenation of a large number of random scatterers would result in a Gaussian distribution of the variation in the dB scale

$$\log(X_1 X_2 X_3 \ldots) = \log X_1 + \log X_2 + \log X_3 + \cdots \tag{19}$$

where $X$ is a random variable representing the scattering coefficient of one bubble. We can further factor out the standard deviation of the random process, and use a standard Normal distribution as the base

$$k_m(t) = k_0 + \sigma_k \zeta(t) \tag{20}$$

where

- $\sigma_k$ standard deviation of the variations of the wavenumber;
- $\zeta(t)$ generic random process with a standard normal distribution and a PSD associated with it.

As the real part of the complex wavenumber is the phase and the imaginary part is the amplitude, we have only three variables to determine; first, $\sigma_a$, the standard deviation of the amplitude variation, second, $\sigma_\theta$, the standard deviation of the phase variation, and third, the PSD of $\zeta(t)$. We extract these statistics from the PN sequence in the wind-wave channel experiment and quantify the impact of this variation on the performance of communication systems.

### B. Propagation and Scattering Conditions During Experiment

In Fig. 11, we show an illustration of the propagation and scattering conditions during the various stages of the experiment. In Stage A, there were no wind and waves, the surface was flat. In Stage B, we turned on the paddle and waves were produced. In Stages C and D, there were a large number of bubbles and in Stage E, there was a long-lasting presence of microbubbles. The waves in Stage B and Stage E were controlled to be identical. The microbubbles that persist caused an increase in channel variability that we intend to quantify.

### C. PN Sequence During Experiment

The PN-sequence probes were in the frequency range of 18–30 kHz, modulated at baseband signaling rate of 12 kbaud with a BPSK modulation scheme. The carrier frequency $f_c$ was centered at 24 kHz. The PN sequence was generated as a maximal length sequence of $m = 9$, with a repetition of $T_{\text{rep}} = 3$, which resulted in $N_c = (2^m - 1)T_{\text{rep}} = 1533$ chips (approximately 120-ms duration). The probe was concatenated with the bubble probes back-to-back as shown in Fig. 2.

### D. Channel Estimation

We match filtered the received and transmitted probes to estimate the channel

$$R_{xy}(\tau) = E\{\tilde{x}(t)\tilde{y}(t-\tau)\} \tag{21}$$

where $x(t)$ is the transmitted probe and $y(t)$ is the received probe, and $\tilde{x}(t)$and $\tilde{y}(t)$ are the Hilbert transforms of those signals. Here, $\tau$ is the time delay. We extracted the amplitude and phase from the output of the matched filter, as the phase and amplitude of each path are the delayed and attenuated copies of

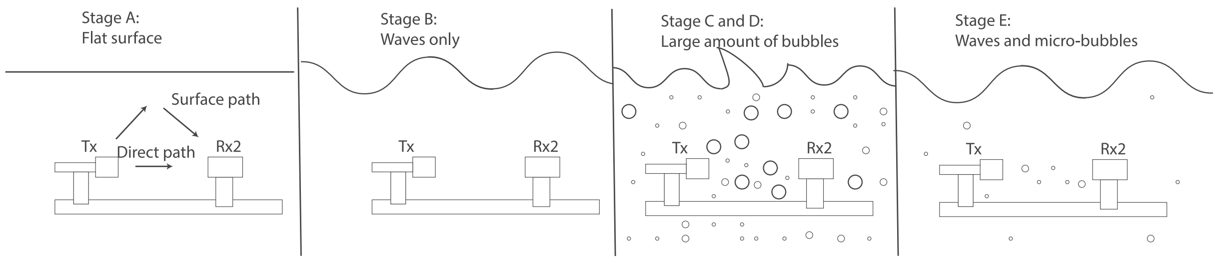


Fig. 11. Illustration of the propagation and scattering conditions during the various stages of experiment (not drawn to scale).

TABLE V
MODEL CALCULATIONS OF PATH ARRIVAL TIME AND OBSERVED ARRIVAL TIME

| Path | Modeled Arrival Time | Observed Arrival Time |
|---|---|---|
| Direct | 0.316/1520 = 0.2 ms | 0.2 ms |
| Surface | $\sqrt{0.316^2 + (0.80)^2}/1520$ =0.6 ms | 0.7 ms |

the autocorrelation function of the transmitted signal

$$R_{xx}(\tau) = E\{\tilde{x}(t)\tilde{x}(t-\tau)\} \tag{22}$$

$$R_{xy}(\tau) = \sum_{p=1}^{P} a_p e^{-j\theta_p} |R_{xx}(t-\tau_p)|. \tag{23}$$

where $a_p$ is the instantaneous amplitude for each path, $\tau_p$ is the arrival time delay for a specific path, and $P$ is the number of discrete paths that had amplitudes above a certain threshold. Furthermore, $\theta_p$ is the residual phase of each path, i.e., $\theta_p = 2\pi f_c \tau_e$, and $\tau_e$ is the excess delay within the minimum resolution.

## E. Choice of Window Length

We balanced the contention between the quality of the channel estimates and the channel sampling rate by specifying the minimum SNR for the application. Subsequently, we determined the corresponding window length required. This length thus limits the sampling rate of the channel. The minimum window length was 12 ms for Rx2. This corresponded to a channel sampling rate of 83 Hz. There was no overlap between the windows. As such, each channel estimate was a snapshot that was independent of the previous one. A good review regarding the tradeoff between the quality of the channel estimate and the channel sampling rate can be found in [39] and [40].

## F. Data Processing

In Fig. 12(a), we show the estimation of the channel at Rx2 during Stage A. The impulse response shows two significant peaks. The two peaks correspond to two different paths. The direct and surface paths are identified by geometry as shown in Table V. Subsequently, in Fig. 12(b), we show a concatenation of the snapshots of the channel during the transition from Stage A to Stage B. We can see that the surface path starts to oscillate when there are waves present, but more importantly, the direct path

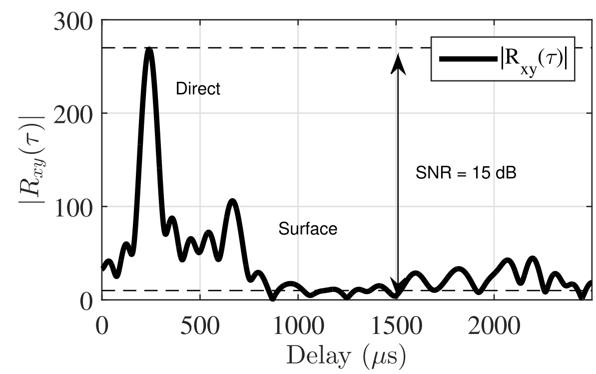


(a)

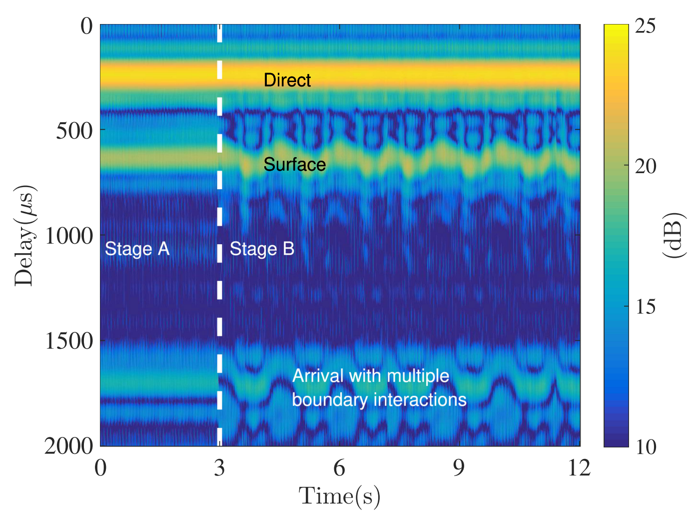


(b)

Fig. 12. (a) Channel estimates of the channel at Rx2 at Stage A. (b) Concatenation of the snapshots of CIRs during the transition from Stage A to Stage B.

is unaffected by wave movements. As such, by extracting the amplitudes and phases from the direct path only, we eliminate the phase and amplitude variations from the moving surface. This allows us to isolate the variations due to transducer motion[1] and bubble motion alone. We extract the amplitude and the phase of the direct path from each channel snapshot as follows:

[1]Although the transducers are rigidly mounted, the mounting structures experience small amount of motion due to changing forces from the waves.

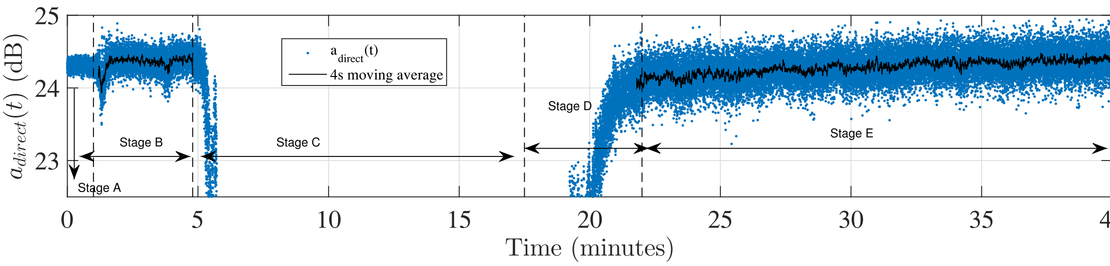


(a)

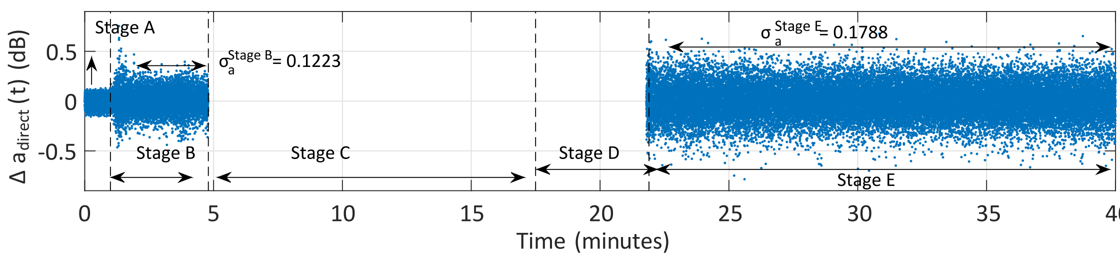


(b)

Fig. 13. Amplitude and amplitude fluctuation of the direct path. Data show the increase in variability during Stage E as compared to Stage B. (a) Amplitude of the direct path during the whole experiment run. On the thin solid line is the 4-s moving average value. (b) Amplitude fluctuations, i.e., $\Delta a(t) = a_{\text{direct}}(t) - \bar{a}_{\text{direct}}(t)$, where $\bar{a}_{\text{direct}}(t)$ is the 4-s moving average.

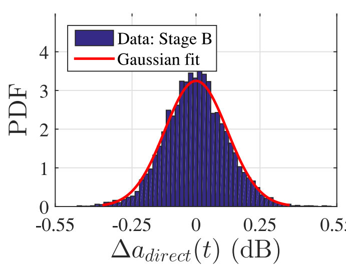


(a)

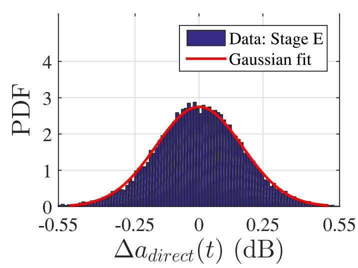


(b)

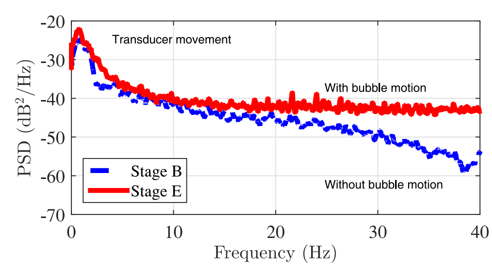


(c)

Fig. 14. Amplitude distribution and PSD of the variations in Stage B and Stage E. From (a) to (b), there is an increase in the width of the distribution following the presence of microbubbles in Stage E. In (c), the data show that there is an increase in variations in the higher frequencies after bubbles were introduced. (a) Amplitude distribution: Stage B. (b) Amplitude distribution: Stage E. (c) Spectral analysis.

1) for every time snapshot $t_n$;
2) find the first maxima in $R_{xy}(\tau, t_n)$ above a threshold and note its corresponding delay time as $\tau_{\text{direct}}$.
3) for $\tau_{\text{direct}}$, assign $a_{\text{direct}}(t_n) = |R_{xy}(\tau_{\text{direct}}, t_n)|$, and $\theta_{\text{direct},t_n} = \angle R_{xy}(\tau_{\text{direct}}, t_n)$;
4) compensate phase associated with delay by: $\theta_{\text{direct},t_n} = (\tau_{\text{direct},t_n} - \tau_{\text{direct},t_0}) 2\pi f_c / \Delta\tau + \angle R_{xy}(\tau_{\text{direct}}, t_n)$, where $\Delta\tau$ is the passband sampling interval.

## *G. Results*

*1) Amplitude Fluctuations:* In Fig. 13(a), initially in Stage A, the variability is low, as the channel is at rest. During Stage B, the variability increases as there are wave-induced transducer motions. At Stage C, the channel is completely blocked. At Stage D, the signal recovers rapidly due to buoyancy. At Stage E, there is a slow recovery due to the dissolution of bubbles. To remove the trend on the longer time scales, we perform a detrend operation with a moving average of 4 s. The results are shown in Fig. 13(b). We observe the variability increase in Stage E, which is due to the propagation through the suspended microbubbles.

We show the amplitude distribution of the direct path in Stages B and E in Fig. 14(a) and (b), respectively. We observe an increase in variability from the data. We compare the data with a fitted Gaussian distribution in the plot. The resulting standard deviation is 0.12 dB for Stage B and 0.18 dB for Stage E. Subsequently, we show the spectral analysis of the amplitude variations in Fig. 14(c). We find that while the time correlations on the 1–10-Hz scale are almost identical (wave-induced transducer motion is consistent), the time correlation from 20 Hz onward is different. This is due to the fast turbulent motion that is randomly transporting the bubbles. We note that the fluctuation is linearly proportional to the intersection length between the path and the plume [41]: $\sigma_a = \sigma_a^0 \, d$, where $\sigma_a^0$ is the normalized variability per meter. For an intersection length of 0.36 m, we measure an increase in standard deviation of 0.06 dB, thus the

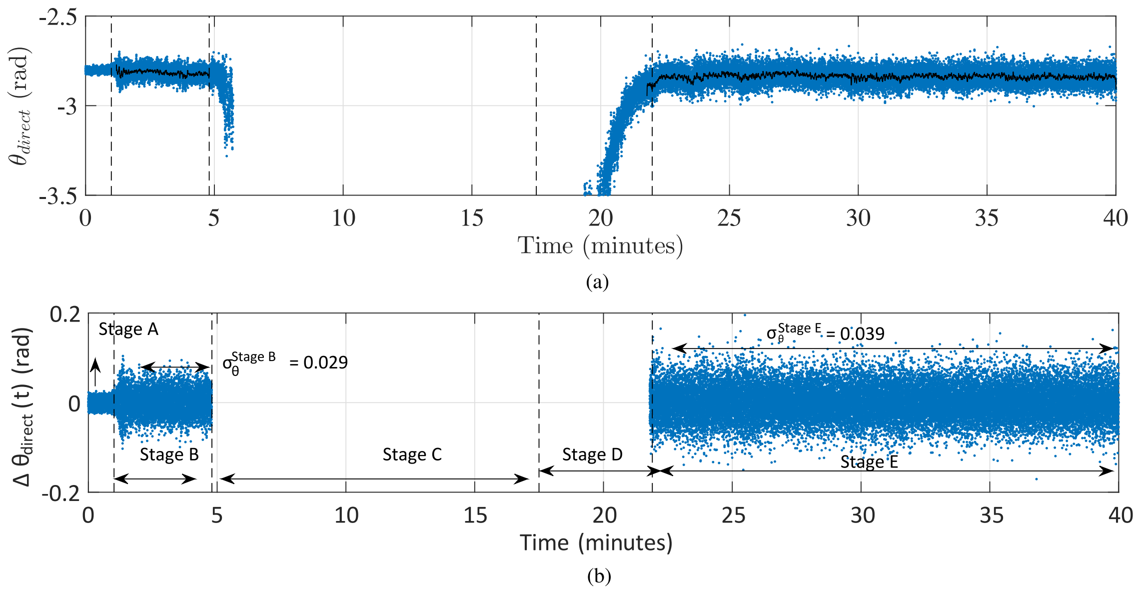


Fig. 15. (a) Extracted phase in radians. (b) Phase fluctuations after the detrend operation. The standard deviation in Stage B is 0.029 and the standard deviation in Stage E is 0.039. One can also see an increase in the variability from Stage B to Stage E. (a) Phase of the direct path during the whole experiment run. The thin solid line is the 4-s moving average value. (b) Phase fluctuations, $\Delta\theta(t) = \theta_{\text{direct}}(t) - \bar{\theta}_{\text{direct}}(t)$, $\bar{\theta}_{\text{direct}}(t)$ is the 4-s moving average.

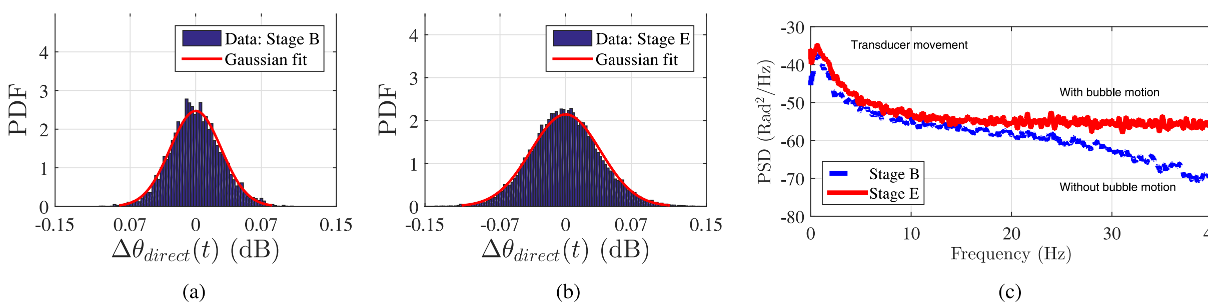


Fig. 16. Phase distribution and PSD of the variations in Stages B and E. (a) Phase distribution: Stage B. (b) Phase distribution: Stage E. (c) Spectral analysis.

variability per meter is estimated to be 0.16 dB/m. In the case of a ship wake plume, an intersecting length of somewhere between $10^0$ and $10^2$ m is possible, depending on channel geometry and plume size. Thus, the possible values of the standard deviation $\sigma_a$ lie somewhere between 0.16 and 16 dB depending on how much the path intersects the plume.

*2) Phase Fluctuations:* Phase variability is shown in Fig. 15(a) and (b). The trend is largely similar to that of the amplitude fluctuation, with the recovery of the phase being attributed to the recovery of the sound speed in the bubbly medium. We perform the detrend operation with a 4-s moving average. The residual phase variability is shown in Fig. 15(b) and 16. Similar to the amplitude fluctuations, we observe an increase in variability in the phase. The phase time correlations exhibit a similar trend to the amplitude time correlations. The increase in standard deviation of the variability is 0.01 rad for 0.36 m, therefore the variability per meter is 0.0278 rad/m. Thus, for a ship wake plume, depending on the intersection length between the path and plume, the increase in variability should lie somewhere between 0.0278 and 2.78 rad.

TABLE VI
DFE Parameters

| Parameter | Value |
|---|---|
| Feedforward taps | 50 |
| Feedback taps | 50 |
| $\mu_{\text{step}}$ | 0.001 |

### H. Impact of Variability on Communication

The communication impact of the microbubbles is shown in Fig. 17. We apply an adaptive DFE with the least mean squares algorithm along with the parameters as shown in Table VI. We measure performance in terms of mean square error (MSE) as follows:

$$\text{MSE} = 10\log_{10}\frac{1}{N_d}\sum_{i=1}^{N_d}|d_i - \hat{d}_i|^2 \tag{24}$$

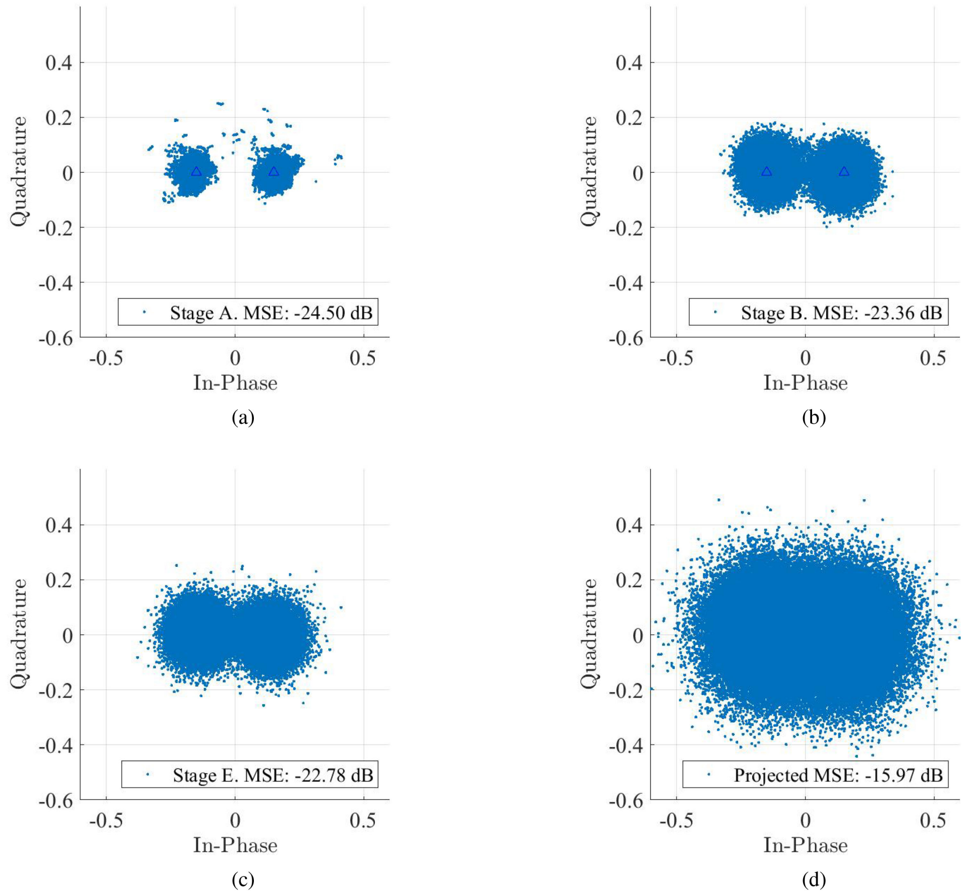


Fig. 17. (a)–(c) Outputs of the DFE after equalization for Stage A, Stage B, and Stage E. (a) Measured: Stage A, no waves, no microbubbles. (b) Measured: Stage B, with waves, no microbubbles. (c) Measured: Stage E, with waves, with microbubbles. (d) Projected variability at an intersection length of 100 m based on the measured variability.

where $d_i$ is the actual symbol transmitted, $\hat{d}_i$ is the soft decision of the equalizer, and $N_d$ is the total number of symbols. In Fig. 17(a)–(c), we show the constellation diagram of the equalized received symbols in Stages A, B, and E, respectively, and we show the MSEs in their respective plots. We observe that although the DFE is able to track the slow variation through the adaptation of the filter coefficients [42], we see that the faster variations are reflected in the MSE; this can be seen as the MSE increases from Fig. 17(a)–(c). In Fig. 17(a), we observe that the MSE is mostly due to inherent noise. In Fig. 17(b), when the waves are being generated, the MSE increases by 0.86 dB due to wave motions. In Fig. 17(c), from Stage B to Stage E, the MSE further increases by 0.58 dB, and this is due to the propagation of the signal through these fast-moving suspended bubbles. The increase in variability is not visually apparent due to the small intersection length. As the length of the channel increases, we expect the variability to increase dramatically. We simulate the projected variability for an intersection length of 100 m to the measured signal and show the results in Fig. 17(d). To eliminate the competing contention between increasing variability and decreasing SNR with the increase in distance, we compensated the SNR in Fig. 17(d) to match the SNR in Fig. 17(c) by increasing the transmitting power. As such, the increase in bit errors in Fig. 17(d) is solely due to the increase in channel variability, which in turn is due to the increase in the number of suspended microbubbles as the intersection length increases.

## VII. Large-Scale Variability

We also observe slow variations that were superimposed on the fast variations as described earlier. The slow variations are attributed to the large-scale advection of the inhomogeneous bubble clouds. As the bubble clouds exist in distinct plumes, the number density of them across space is largely inhomogeneous. As these bubbles clouds are being transported by the currents on a periodic basis in the channel, they produce time correlations of the signal on a few minutes interval. We illustrate this effect with the data from Rx3.

### A. *Channel Impulse Response (CIR)*

We show the CIR measured at Rx3 in Fig. 18. We predict the arrival time of each path and match it with the experimentally observed arrivals (see Table VII). We then label the paths to the arrivals in Fig. 18.

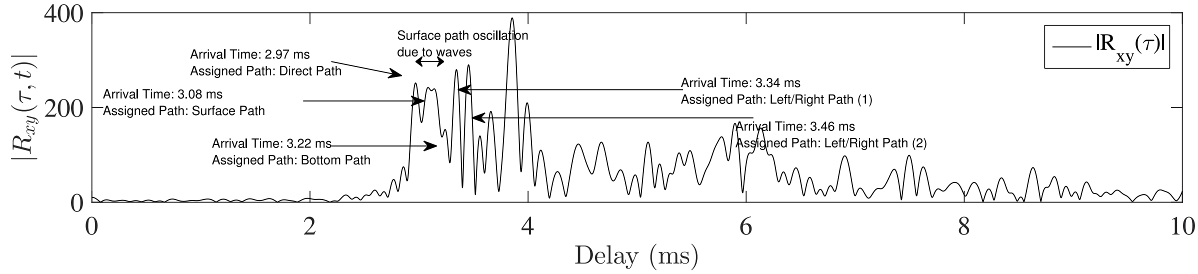


Fig. 18. CIR at Rx3 when the channel is static initially. On the labels are assigned paths of each arrival based on calculations from the channel geometry. On the upper double arrow is the movement of the surface path when the waves are on. As wave height is 0.35 m peak to peak, this corresponds to $\approx 0.23$ ms delay time fluctuation.

TABLE VII
MODEL CALCULATIONS OF IMPULSE RESPONSE ARRIVAL TIME VERSUS EXPERIMENT OBSERVED ARRIVAL TIME

| Path | Model Arrival Time (Method of Mirror) | Observed Arrival Time |
|---|---|---|
| Direct | 4.63/1520 = 3.03 ms | 2.97 ms |
| Surface | $\sqrt{4.63^2 + 2(0.40)^2}/1520 = 3.09$ ms | 3.08 ms |
| Bottom | $\sqrt{4.63^2 + 2(0.80)^2}/1520 = 3.22$ ms | 3.22 ms |
| Left/Right path(1) | $\sqrt{4.63^2 + 2(1.15)^2}/1520 = 3.40$ ms | 3.34 ms |
| Left/Right path(2) | $\sqrt{4.63^2 + 2(1.15)^2}/1520 = 3.40$ ms | 3.46 ms |

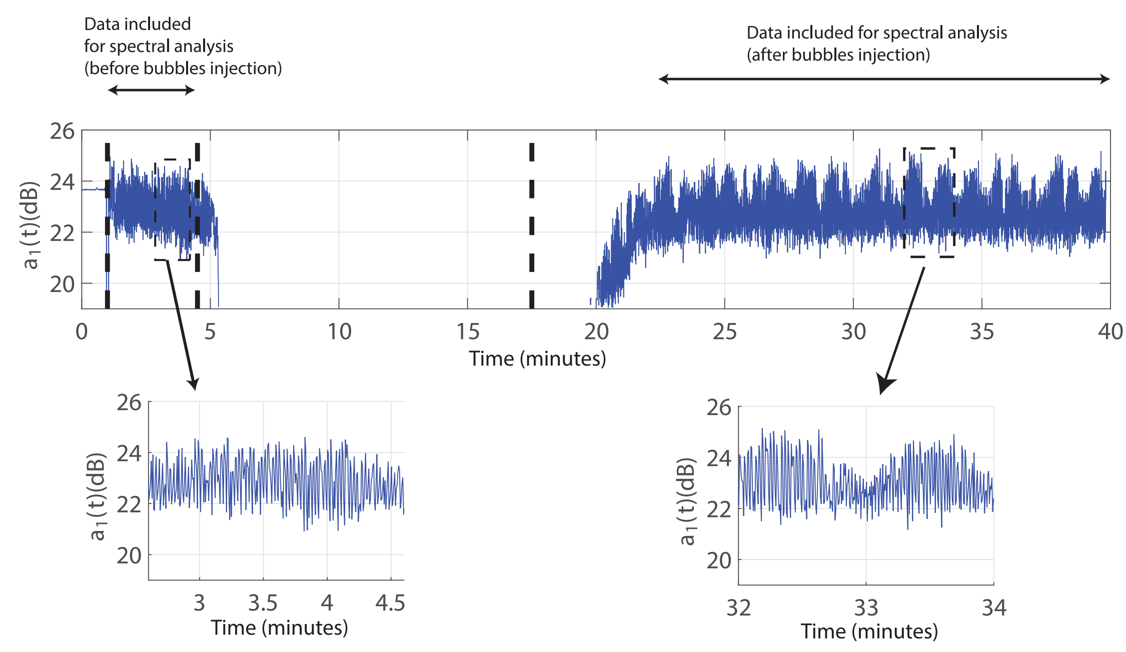


Fig. 19. In the upper panel, we show the amplitude of the first most energetic arrival at Rx3 for all the channel snapshots across the time frame of 40 min. On the two lower panels, we show an enlarged view of the variations in a time frame of 2 min for both before and after the injection. We observe that while the oscillation on a 2-s interval is largely similar, the modulating envelope on a minute-to-minute basis is distinctly different.

## B. Data Processing

As the first cluster of arrival is a mixture of the surface and direct paths, we dub this cluster the first most energetic arrival $a_1(t)$. In Fig. 19, we depict $a_1(t)$ throughout the experiment. In Stage A, the amplitude had very little variation. Subsequently, in Stage B, the amplitude starts to fluctuate. Upon examining the cyclic structure of the fluctuations, we note that the natural frequency of the fluctuations is almost identical to the natural frequency of the waves, suggesting that the cyclic fluctuation is mostly due to waves. The wave motion is integrated into the arrival because the time separation of the direct path and surface

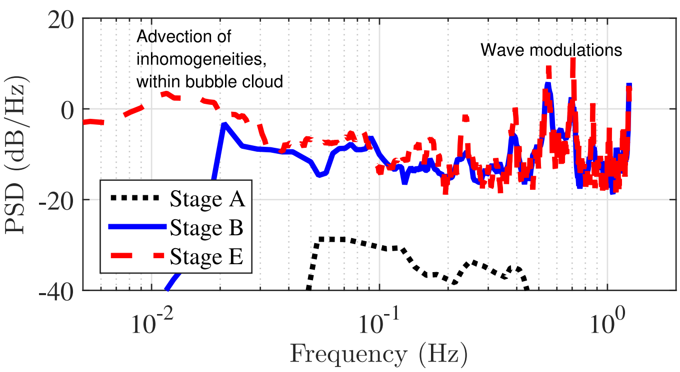


Fig. 20. PSD of the variations. On the blue solid line is the spectrum at Stage B (only waves), and on the red dashed line is the spectrum at Stage E (waves and microbubbles advection). On the black line is the spectrum in Stage A (electrical noise only). The wave modulation remained the same, but the subhertz band is distinctly different.

path is less than the delay time fluctuation caused by the wave motion. In Stages C and D, the attenuation was high. Then at Stage E, we observe that the signal strength recovers to a steady state. The wave modulation patterns remained the same, as the waves were controlled to be identical throughout the experiment. More importantly, we note that the modulating envelope on a longer time scale is distinctly different. We attribute this to the advection of the inhomogeneous structure of the bubble clouds.

### C. Spectral Analysis

We show the spectral analysis of the signal at Stages A, B, and E in Fig. 20. The variations at Stage A is small, the power of the variations is at a level of about −40 dB. Furthermore, the spectral components due to the surface waves at 0.3–0.8 Hz are identical in Stages B and E (waves were controlled). More importantly, we observe the larger spectral component at the lower frequencies from 0.1 to 0.01 Hz, and we attribute this to the advection of bubble clouds, which have inhomogeneous bubble population in them. We observe that they have correlation time scales in the order of minutes.

### D. Mitigation

Since we observe a correlation time scale in the order of minutes, adaptive modulation may be used to mitigate against ill effects of bubbles. Adaptive modulation requires that the channel coherence time exceeds the round-trip delay time by a few orders of magnitude [43]. For a typical deployment range of a few kilometers, the round-trip propagation time is in the order of seconds, whereas the correlation time scale of the large-scale advection of bubbles is in the order of minutes. This opens up opportunities for channel conditions to be fed back to the transmitter for the scheme to be tuned accordingly.

## VIII. Conclusion

We designed an experiment to understand the impact of bubbles on acoustic communication. We found that after a bubble injection event, the high attenuation due to dense bubble clouds typically lasted a few minutes, during which the larger bubbles rose up to the surface through buoyancy. Eventually, there was a portion of small bubbles that were suspended and remained in the water for long periods. During this phase, the bubble lifetime was governed by dissolution, a much slower process than buoyancy. These bubbles lasted longer and caused a more persistent impact on communication.

The suspended microbubbles can last for hours if the bubbles are stabilized by "dirty" seawater. As the spatial effect of these bubbles can be extended as far as the currents can carry them during their long lifetimes, the suspended microbubbles can have an impact in places quite far from the sources of these bubbles.

The attenuation effects of the suspended microbubbles depend on both the size of the bubbles that are suspended and the acoustic frequency deployed. For frequencies lower than the resonance of the largest suspended bubble, although attenuation from the suspended microbubbles is usually small, these subresonance bubbles act as random moving scatterers and increase channel variability. We provided a statistical characterization of the variability in terms of its amplitude and phase distribution, as well as their time correlation. The performance of communication algorithms in such elevated variability channels is poorer, unless the algorithms specifically address the time variability. The understanding of the generation and dissipation mechanism of bubbles can enable the practitioner to design communication systems catered for the specific environment.

## Acknowledgment

The authors would like to express their gratitude to O. L. Lin for proofreading an initial version of this article.

## References

[1] G. B. Deane, "Acoustic hot-spots and breaking wave noise in the surf zone," *J. Atmos. Ocean. Technol.*, vol. 105, pp. 3151–3167, 1999.

[2] E. C. Monahan, *Natural Physical Sources of Underwater Sound: A Model for Variations in the Range and Depth Dependence of the Sound Speed and Attenuation Induced by Bubble Clouds Under Wind-Driven Sea Surfaces*, B. R. Kerman, Ed. Boston, MA, USA: Kluwer, 1993.

[3] J. Novarini, R. Keiffer, and G. Norton, "A model for variations in the range and depth dependence of the sound speed and attenuation induced by bubble clouds under wind-driven sea surfaces," *IEEE J. Ocean. Eng.*, vol. 23, no. 4, pp. 423–438, Jan. 1998.

[4] C. A. Boyles, A. P. Rosenberg, and Q. Zhang, "Modeling the effect of bubble plumes on high frequency acoustic propagation in shallow water," in *Proc. IEEE/MTS OCEANS Conf.*, San Diego, CA, USA, 2013, pp. 1–8.

[5] K. Saraswathi, S. Ravishankar, and V. Singh, "Underwater communications in the presence of bubbles and doppler shift," in *Proc. Int. Conf. Adv. Comput., Commun. Inform.*, 2017, pp. 2173–2179.

[6] A. K. Mandal, S. Misra, T. Ojha, M. K. Dash, and M. S. Obaidat, "Effects of wind-induced near-surface bubble plumes on the performance of underwater wireless acoustic sensor networks," *IEEE Sensors J.*, vol. 16, no. 11, pp. 4092–4099, Jun. 2016.

[7] H. S. Dol, M. Colin, M. Ainslie, P. A. Walree, and J. Janmaat, "Simulation of an underwater acoustic communication channel characterized by wind-generated surface waves and bubbles," *IEEE J. Ocean. Eng.*, vol. 38, no. 4, pp. 642–654, Oct. 2013.

[8] C. A. Boyles, A. P. Rosenberg, and Q. Zhang, "Underwater acoustic communication channel characterization in the presence of bubbles and rough sea surfaces," in *Proc. OCEANS Conf.*, Spain, 2011, pp. 1-8.

[9] P. A. Walree, "Propagation and scattering effects in underwater acoustic communication channels," *IEEE J. Ocean. Eng.*, vol. 38, no. 4, pp. 614–631, Oct. 2013.

[10] D. Farmer, G. Deane, and S. Vagle, "The influence of bubble clouds on acoustic propagation in the surf zone," *IEEE J. Ocean. Eng.*, vol. 26, no. 1, pp. 113–124, Jan. 2001.
[11] P. H. Dahl, W. J. Plant, B. Nutzel, A. Schmidt, H. Herwig, and E. A. Terray, "Simultaneous acoustic and microwave backscattering from the sea surface," *J. Acoust. Soc. Amer.*, vol. 110, no. 5, 1997, Art. no. 2583.
[12] P. H. Dahl, J. W. Choi, N. J. Williams, and H. C. Graber, "Field measurements and modeling of attenuation from near-surface bubbles for frequencies 1-20 kHz," *J. Acoust. Soc. Amer.*, vol. 124, no. 3. pp. EL163–E169, 2008.
[13] P. H. Dahl, "The contribution of bubbles to high-frequency sea surface backscatter: A 24-h time series of field measurements," *J. Acoust. Soc. Amer.*, vol. 113, no. 2, pp. 769–780, 2003.
[14] M. Stojanovic, J. A. Catipovic, and J. G. Proakis, "Phase-coherent digital communications for underwater acoustic channels," *IEEE J. Ocean. Eng.*, vol. 19, no. 1, pp. 100–111, Jan. 1994.
[15] N. Carbone and W. S. Hogdkiss, "Effects of tidally driven temperature fluctuations on shallow-water acoustic communications at 18 kHz," *IEEE J. Ocean. Eng.*, vol. 25, no. 1, pp. 84–94, Jan. 2000.
[16] A. Song, M. Badiey, S. H. C., W. S. Hogdkiss, and M. B. Porter, "Impact of ocean variability on coherent underwater acoustic communications during the Kauai experiment (Kauaiex)," *J. Acoust. Soc. Amer.*, vol. 123, no. 2, pp. 856–865, 2007.
[17] P. A. Walree, N. A. Jeffrey, and M. C. Schrijver, "Coherent acoustic communication in a tidal estuary with busy shipping traffic," *J. Acoust. Soc. Amer.*, vol. 122, no. 1, pp. 3495–3506, 2007.
[18] G. Chua, M. Chitre, and G. Deane, "Impact of persistent bubbles on underwater acoustic communication," in *Proc. 4th Underwater Commun. Netw. Conf.*, 2018.
[19] T. Leighton, *The Acoustic Bubble*. New York, NY, USA: Academic, 1994.
[20] H. Medwin and C. S. Clay, *Acoustical Oceanography*. Hoboken, NJ, USA: Wiley, 1977.
[21] H. Medwin and C. S. Clay, *Fundamentals Acoustical Oceanography*. New York, NY, USA: Academic, 1998.
[22] H. Czerski, "An inversion of acoustical attenuation measurements to deduce bubble populations," *J. Atmos. Ocean. Technol.*, 29, pp. 1139–1148, 2012.
[23] R. Wildt, "Physics sound the sea," National Def. Res. Committee, Washington, DC, USA, Tech. Rep. Div. 6, vol. 8, 1949.
[24] H. Medwin, "In situ acoustic measurements of bubble populations in coastal ocean waters," *J. Geophys. Res*, vol. 75, no. 1, 1970, Art. no. 599611.
[25] H. Medwin, "In situ acoustic measurements of microbubbles at sea," *J. Geophys. Res*, vol. 82, no. 6, pp. 971–976, 1977.
[26] H. Medwin, "Acoustical determination of bubble size spectra," *J. Acoust. Soc. Amer.*, vol. 62, pp. 1041–1044, 1977.
[27] S. Stanic, J. Caruthers, R. R. Goodman, E. Kennedy, and R. A. Brown, "Attenuation measurements across surface-ship wakes and computed bubble distributions and void fractions," *IEEE J. Ocean. Eng.*, vol. 34, no. 1, pp. 83–92, Jan. 2009.
[28] N. Breitz and H. Medwin, "Instrumentation for *in-situ* acoustical measurements of bubble spectra under breaking waves," *J. Acoust. Soc. Amer.*, vol. 86, pp. 739–743, 1989.
[29] S. Vagle and D. Farmer, "A comparison of four methods for bubble size and void fraction measurements," *IEEE J. Ocean. Eng.*, vol. 23, no. 3, pp. 211–222, Jul. 1998.
[30] P. S. Epstein and M. S. Plesset, "On the stability of gas bubbles in liquid-gas solutions," *J. Chem. Phys.*, vol. 18, pp. 1505–1509, 1950.
[31] K. George and P. H. Dahl, "Scattering measurements from a dissolving bubble," *J. Acoust. Soc. Amer.*, vol. 131, pp. 4243–4251, 2012.
[32] B. D. Johnson and P. J. Wangersky, "Microbubbles: Stabilization by monolayers of adsorbed particles," *J. Geophys. Res.*, vol. 92, no. C13, pp. 14641–14647, 1987.
[33] J. W. Cartmill and Y. S. Ming, "Bubble size distribution under saltwater and freshwater breaking waves," *Dyn. Atmos. Oceans*, vol. 20, pp. 25–31, 1993.
[34] G. Chua, "The impact of bubbles on underwater acoustic communication," Ph.D. dissertation, Dept. Elect. Comput. Eng., Nat. Univ. Singapore, Singapore, 2020.
[35] L. Foldy, "The multiple scattering of waves," *Phys. Rev.*, no. 67, pp. 107–119, 1945.
[36] K. Commander and A. Prosperetti, "Linear pressure waves in bubbly liquids: Comparison between theory and experiments," *J. Acoust. Soc. Amer.*, vol. 85, no. 2, 1989, Art. no. 732.
[37] S. A. Thorpe, "Bubble clouds and the dynamics of the upper ocean," *J. Roy. Meteorol. Soc.*, vol. 118, no. 503, pp. 1–22, 1992.
[38] G. P. Gerbi, "Observations of turbulence in the ocean surface boundary layer: Energetics and transport," *J. Phys. Oceanogr.*, vol. 39, pp. 1077–1096, 2009.
[39] P. A. Walree, T. Jenserud, and S. Smedsrud, "A discrete-time channel simulator driven by measured scattering functions," *IEEE J. Sel. Area Commun.*, vol. 26, no. 9, pp. 1628–1637, Dec. 2008.
[40] P. A. Walree, "Channel sounding for acoustic communications: Techniques and shallow-water examples," Norwegian Def. Res. Establishment (FFI), Kjeller, Norway, Tech. Rep. FFI-rapport 2011/00007, 2011.
[41] R. W. Lee and J. C. Harp, "Weak scattering in random media, with applications to remote probing," *Proc. IEEE*, vol. 57, no. 4, pp. 375–406, Apr. 1969.
[42] T. H. Eggen, "Underwater acoustic communication over Doppler spread channels," Ph.D. dissertation, Dept. Elect. Eng. Comput. Sci., Massachusetts Inst. Technol., Cambridge, MA, USA, 1997.
[43] P. Qarabaqi and M. Stojanovic, "Adaptive power control for underwater acoustic communications," in *Proc. OCEANS Conf.*, Spain, 2011, pp. 1–7.

**Gabriel Chua** (Student Member, IEEE) received the B.Eng. and M.Sc. degrees in electrical engineering and the Ph.D. degree in underwater communications from the National University of Singapore (NUS), Singapore, in 2009, 2012, and 2020, respectively.

From 2014 to 2020, he was a Research Engineer with the Acoustic Research Laboratory, NUS and was promoted to a Research Fellow in 2020. His research interests include underwater communications, acoustic propagation modeling, and upper ocean physics.

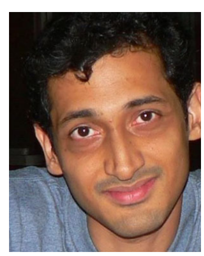

**Mandar Chitre** (Senior Member, IEEE) received the B.Eng. and M.Eng. degrees in electrical engineering from the National University of Singapore (NUS), Singapore, in 1997 and 2000, respectively, the M.Sc. degree in bioinformatics from Nanyang Technological University, Singapore, in 2004, and the Ph.D. degree in underwater communications from NUS, in 2006.

From 1997 to 1998, he was with the Acoustic Research Laboratory (ARL), NUS. From 1998 to 2002, he was the Head of the Technology Division of a regional telecommunications solutions company. In 2003, he rejoined ARL initially as the Deputy Head (Research), where he is currently the Head of the Laboratory. He also holds a joint appointment with the Department of Electrical and Computer Engineering, NUS, as an Associate Professor. His research interests include underwater communications, acoustic signal processing, acoustic propagation modeling, and marine robotics.

**Grant B. Deane** received the B.Sc. and M.Sc. (Hons.) degrees in physics from Auckland University, Auckland, New Zealand, in 1982 and 1983, respectively, and the D.Phil. degree in mathematics from Oxford University, Oxford, U.K., in 1989.

From 1990 to 1992, he was a Mellon Fellow at the Scripps Institution of Oceanography (SIO), University of California at San Diego, La Jolla, CA, USA. He has been a Research Oceanographer with SIO since 1995. His research interests include underwater acoustics, small.]scale, upper ocean physics (wave breaking, turbulence, air entrainment, and marine aerosol generation), and ambient noise cryology.

Dr. Deane is a Fellow of the Acoustical Society of America and a member of the American Geophysical Union, the American Meteorological Society, and The Oceanography Society.